JOURNAL OF PROPULSION AND POWER
Vol. 15, No. 3, May–June 1999

Experimental Investigation of the Role of Downstream Ramps on a Supersonic Injection Plume

Mark P. Wilson*
Air Force Institute of Technology, Wright–Patterson Air Force Base, Ohio 45433-7765
Rodney D. W. Bowersox†
University of Alabama, Tuscaloosa, Alabama 35487-0280
and
Diana D. Glawe‡
U.S. Air Force Research Laboratory, Wright–Patterson Air Force Base, Ohio 45433-7301

An experimental study was conducted to investigate penetration and plume expansion enhancement of a discrete low-angled (25 deg) supersonic ($M = 1.9$) injection into a supersonic ($M = 2.9$) crossflow. The enhancement was achieved by injecting the low-angled jet parallel to a compression ramp. Seven compression ramp configurations were studied. The jet-ramp interaction enhancement mechanisms included baroclinic torque vorticity, ramp spillage vorticity, bulk compression, and the Magnus force. Shadowgraph photography was used to identify shock structures. Measurements of mean flow properties quantified the flowfield total pressure losses. Mie scattering images were used to qualitatively assess the flowfield and to quantify the plume size, trajectory, and concentration decay rate. The results indicated that up to a 22% increase in penetration, a 39% plume expansion (~mixing), and a 27% increase in the concentration decay rate, with a corresponding 17% increase in total pressure loss, can be achieved by injection over a compression ramp as compared with low-angled injection alone.

Nomenclature

A_b = ramp blockage area
A_p = Mie scattering image injectant plume area
D = decay rate [$dI^*/d(x/d)$, Fig. 6]
d = injector port minor axis diameter
I^* = normalized scattered intensity
p_{eb} = effective back pressure
p_j = jet exit pressure
P_{t0} = undisturbed freestream total pressure
P_{t1} = local total pressure
$\bar{q}$ = jet-to-freestream momentum ratio
x, y, z = Cartesian coordinate system
y_m = maximum penetration at $x/d = 20$, Fig. 5
δ = boundary-layer thickness
λ = expansion ratio, p_j/p_{eb}
ξ_y = $\{[(\,)|_{\text{Ramp}} - (\,)|_{\text{No Ramp}}]/(\,)|_{\text{No Ramp}}\}/(1 - \Pi)$
Π = total pressure ratio, Eq. (1)

Introduction

THE development of a hypersonic air-breathing propulsion system offers many technological challenges. For example, slowing hypersonic flow to subsonic speeds for combustion would produce prohibitively high temperatures. The scramjet alleviates the requirement to slow the incoming airstream to subsonic velocities. However, combustion at supersonic speeds poses its own challenges, for example, how to manage efficient mixing and burning of the fuel during the extremely short residence time of the working fluid in the combustor. Thus, the optimization of fuel-injection schemes is essential to the development of a scramjet propulsion system.

Several schemes have been employed during the last 30 years to enhance the penetration and mixing of a gas injected into a supersonic stream.[1–12] In an effort to provide a basis of comparison between studies under diverse conditions, several injection parameters and flow variables have been established. The injection parameters include injector-to-freestream ratios such as the velocity ratio, mass flux ratio, expansion ratio (λ), and the dynamic pressure ratio ($\bar{q}$). The expansion ratio is defined as jet exit pressure to effective back pressure (p_{eb}) ratio.[1,2] Where ramps are involved, a standard set of geometric parameters arise such as the ramp height to injector port diameter ratio, the ramp wedge angle, and the angle of sweep of the ramp vertical sides. The primary flow variables of concern for this type of study are the Reynolds-number-based injector diameter, the boundary-layer thickness to injector diameter ratio, and the flow total properties.

Perpendicular injection of an underexpanded sonic or supersonic jet into a supersonic freestream produces several flow structures. The first of these is a bow shock produced as the freestream impacts the injection stream tube; in this respect, the injectant acts as a solid cylindrical body.[3] For injector configurations where δ/d is on the order of one or more, a separation region and a lambda shock form slightly upstream of the injector port.[2,3] After entering the freestream, the jet experiences a rapid Prandtl–Meyer expansion (usually assumed to be an isentropic process), surrounded by a barrel shock.[4] A shock normal to the jet path, known as the Mach disk, terminates the barrel shock, and compresses the flow to p_{eb}. Before the Mach disk, the injectant and freestream are typically treated as separate entities; afterward, vorticity and other turbulent mechanisms induce large-scale mixing between the jet fluid and the freestream.

Angled injection is a means of reducing total pressure loss. Further, low-angle injection has been shown to create a measurable increase in the overall combustion thrust potential,[5,6] as compared with normal injection. In either normal or angled injection, the entry of the injectant jet into the mainstream flow can be regarded as a two-stage process.[2] The jet first enters the main flow and remains relatively intact as it expands to the height of the Mach disk. Beyond the Mach disk, the flow turns coaxial to, and accelerates with, the main flow. In the second stage, the jet acts as a coaxial vortex mixing structure. In the near field, $\bar{q}$ has been shown to strongly affect

Received Nov. 8, 1997; revision received Aug. 21, 1998; accepted for publication Oct. 1, 1998.

*Graduate Research Assistant, Department of Aeronautics and Astronautics.
†Assistant Professor, Department of Aerospace Engineering and Mechanics. Senior Member AIAA.
‡Experimental Research Engineer, Propulsion Directorate. Member AIAA.

mixing and penetration. Penetration is enhanced with increasing $\bar{q}$, in that the Mach disk is pushed farther out into the freestream; however, the plume then turns more sharply with the main flow.[2] This effect was seen to diminish with increasing $\bar{q}$.[2] The initial mixing rate has been documented to be proportional to $1/\bar{q}$.[7] In the far field, $\bar{q}$ has been shown to have little impact on mixing rates.[7,8] A benefit from increasing $\bar{q}$ for low injection angles is a decrease in total pressure loss from the added streamwise component of jet momentum.[8]

The effect of the injection angle on near-field injectant penetration and mixing has received surprisingly little attention to date. However, the available far-field results show that the mixing rates are correlated by the decay of maximum injectant concentration. As the angle of injection is increased, holding all other flow variables and injection parameters constant, far-field mixing rates increase.[7] In conjunction with the far-field mixing increase, there is an unfavorable increased bow shock strength and total pressure loss.[7]

Physical ramps have been shown to increase the mixing efficiency. Two benefits are realized by injecting through a ramp. First, the ramp provides significant vortex generation for mixing and penetration of the injectant jet. Second, behind the rear surface of a ramp is a relatively slow-moving recirculation zone, which would act as a flameholder in a combustor. The ramps explored so far have relatively low wedge angles, ranging from 9.5 to 10.3 deg.[8–12] The injectant jet usually exits normal to the rear face at the wedge angle. Though the generic underexpanded jet structures are present, there are additional ramp base effects, including multiple three-dimensional shocks and expansions, which impact the flow structure. This region of the flow is highly three dimensional and turbulent; not all of the interactions and flow mechanics have been completely mapped or explained. Beyond the ramp base, the plume shape becomes somewhat similar to that of a low-angled injection, with the exception of a stronger vortex pair.

Regardless of the injection scheme employed, vorticity is the driving mixing mechanism in the near field.[3] In transverse injection, a streamwise counter-rotating vortex pair within the jet plume is generated by viscous shearing around the periphery of the jet as the freestream fluid wraps around the plume near the injection port. The pressure differential across the emerging and turning jet that produces downstream entrainment also adds to the strength of the counter-rotating vortex pair within the plume.

For ramp injection, the primary vortex generation comes from the ramp, not the injectant plume, where pressurized fluid in the shock layer between the ramp bow shock and compression face spills around the ramp, creating streamwise vorticity.[9,10] Additional vorticity is imparted by the pressurized flow expanding over the rear face of the ramp and wrapping around the low-pressure region encircling the underexpanded jet plume.[11] Side-wall sweep has been shown to increase vorticity and combustion efficiency.[9,12] A final ramp-induced vortex mechanism is baroclinic torque created by passing a shock through the jet and different density surrounding crossflow.[5]

Once the counter-rotating vortex pair is generated, it becomes the dominant mixing mechanism in the near field.[3,5] For both transverse and ramp injection, the cross-sectional view of the developed plume remains nominally circular, with a kidney bean[13] or cardioidal structure forming around the vortex cores. At some point in the downstream flow, mixing becomes dominated by small-scale turbulence as the vortex strength is dissipated. Hollo et al.[3] found this length to be about $10d$ for tandem normal injectors in Mach 2.0 flow; this distance would increase for lower injection angles and higher velocities. Vorticity also has an effect on penetration, where the vortex pair provides a liftoff from the near wall as a result of a Magnus effect.[5,10]

The primary focus of this study was to experimentally examine the potential increases in near-field penetration and mixing of a low-angled injection into a supersonic crossflow by placing a physical ramp just downstream of the injection port. The interactions between the counter-rotating vortex pair and the ramp surfaces provide a means to passively control the plume structure. For the present study, a Mach 1.9 underexpanded supersonic airjet was injected at 25 deg into a Mach 2.9 air freestream. Figure 1 shows the basic geometry of the present injector–ramp configuration. In the present study, seven different penetration and mixing enhancement (PME) ramps were investigated.

Table 1 Freestream flow conditions[a]

Condition	M	P, kPa	T, K	U, m/s	λ	$\bar{q}$
Freestream	2.9	6.9	110	610	——	——
Injector	1.9	47.6	170	490	3.5	2.8

[a]Nominal 2.0% variation in the flow total conditions.

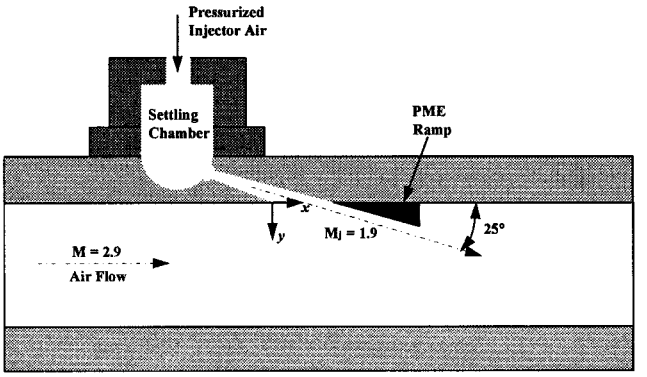

Fig. 1 Schematic of wind-tunnel setup (not to scale).

Facilities

All tests were performed in a supersonic wind tunnel located at Wright–Patterson Air Force Base. The freestream Mach number was 2.88 ± 0.03, and the total pressure and temperature were maintained at 203 ± 3.0 kPa and 294 ± 2 K, respectively. The freestream Re/m was 17×10^6. The freestream turbulent kinetic energy was 0.03% of the freestream mean specific kinetic energy. The test section was 6.35×6.35 cm in cross section. The transverse injector model was mounted into the tunnel ceiling as shown in Fig. 1. For the present study, air was injected at 25 deg, through a Mach 1.9 convergent–divergent conical nozzle into a freestream of air. The coordinate system is also defined in Fig. 1. A complete description of the injector is given in Ref. 14. The exit port was elliptical with a 3.9-mm minor axis (d) and a 9.1-mm major axis. The injector total pressure and temperature were maintained at 314 ± 3.0 kPa and 294 ± 2 K. The freestream boundary-layer thickness at the injector port (without injection) had a height of $1.6d$. Table 1 summarizes the flow conditions for the present study.

Penetration and Mixing Enhancement Ramps

The PME ramp-injection scheme was devised to capitalize on inherent plume features (specifically, the counter-rotating vortex pair), to provide a passive means to control the plume structure. The basic idea was that the solid boundary of the PME ramp compression face would delay the turning of the plume; thus, enhancing penetration as well as increasing the vertical height so that the freestream would be able to add more vorticity to the plume. The solid boundaries and the plume vortex pair should also couple to increase penetration via the Magnus force. Additionally, as the freestream fluid wraps and recompresses around the jet, a region of high pressure should be created between the jet plume and the ramp compression face (bulk compression), which would increase penetration. The increased streamwise vorticity created by the PME ramps provide a means to enhance near- and far-field mixing. The shocks and expansions generated by the ramps also provide a mechanism, the baroclinic torque, to control the plume vorticity and mixing. As an additional benefit, it is also conceivable that the ramps could be designed to produce a high-pressure recirculation region with near stoichiometric fuel–air mixture for flameholding.

The three PME ramp groups (symmetric, extended, and asymmetric), defined in Fig. 2, were examined. A no-ramp injection case was included for comparative purposes. The leading-edge compression

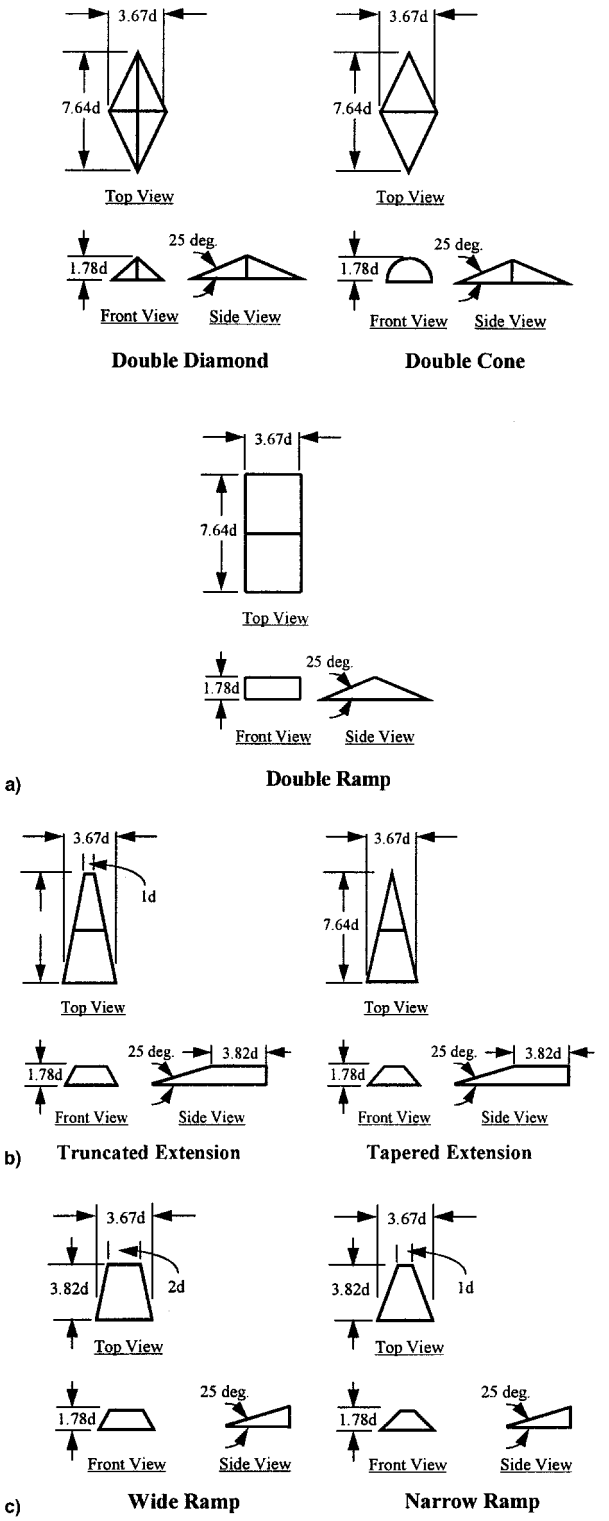

Fig. 2 PME ramp geometry schematics (not to scale): a) symmetric, b) extended, and c) asymmetric ramps.

face for each ramp matched the 25-deg jet exit angle, and the ramps were positioned just downstream of the injector exit port; it was assumed that these two measures would minimize the strength of the ramp-generated shocks, thus, minimizing the increased total pressure loss (wave drag) created by the ramps. In addition, in high-enthalpy flows, this injection scheme could also provide effective film cooling of the ramps, which otherwise might not survive the harsh combustor environment. The present ideology may not lead to the optimum fuel-injection scheme; ramp position and leading-edge compression angle may also be important design parameters. Further, if the ramps are positioned somewhat farther downstream, they may also be useful penetration and mixing enhancement devices for physical ramp injectors. However, the scope of the present study was limited to the configuration shown schematically in Fig. 1.

The symmetric ramps (group I) are shown in Fig. 2a. The double diamond, double cone, and double ramp each presented a progressively broader surface for the bulk compression and Magnus force penetration and baroclinic torque vorticity-generated mixing enhancement. Each ramp in this group generated a different-shaped shock, which generated a different level of baroclinic torque vorticity. Similar to the shock effect, each model in the symmetric ramp group also produced a different-shaped corner expansion, which also influenced the baroclinic torque-generated vorticity.

The extended ramps (group II), depicted in Fig. 2b, were designed such that the injectant plume and freestream would pressurize the upper surfaces of the PME ramp, and induce the spillage-generated vorticity. In addition, the ramp extensions produced a weaker expansion as compared with the symmetric ramps (discussed in the next paragraph). Further, the solid extensions provided a barrier to inhibit migration of the plume back toward the injection wall. Any impingement of the plume on the extension was expected to generate Magnus force lift from the plume vortices.

The asymmetric ramps (group III) consisted of the wide and narrow asymmetric ramps shown in Fig. 2c. Similar to the extended ramp group, spillage-generated vorticity was expected to enhance the transverse injection vorticity. The principal difference between this group and group II was the absence of the extended trailing edges. Thus, the influence of the expansion strength as compared with the group II ramps was evaluated. The different angles of sweep on the ramp sides allowed for an assessment of ramp-generated vorticity on the plume properties.

Because of space constraints, the flowfield descriptions presented in this paper are confined to the three ramp configurations that produced the most profound affect on the plume cross-sectional area. The three configurations chosen were the double, tapered, and wide ramps (see Fig. 2). Because each of the three ramp classifications is represented by one of the three chosen ramps, only describing the results for the three indicated ramps is not considered a limitation. Performance results for all seven ramps are presented here, and detailed flowfield analyses for all seven are given by Wilson.[16]

Instrumentation and Data Analysis

Instantaneous shadowgraph images were obtained using a xenon 10-ns pulse system. The images were recorded on Polaroid type 57 film. Conventional pitot and 10 deg $\pm$ 0.03 deg semivertex angle cone-static probes were used to measure the local Mach number and total pressure. The Mach number was computed from the measured cone-static and pitot pressure by using the Rayleigh–pitot formula and Taylor–Maccoll conical flow theory.[14,15] Contours were obtained at $x/d = 20$, by making vertical traverses across the test section from $y/d = 0.4$ to 11.5. The profiles were acquired at 29 stations (0.164 cm apart), covering a z/d range from -5.6 to 5.6. The probes were traversed at 10 mm/s. The data were sampled at 400 Hz, and 40 point averages were computed.

The total pressure ratio P_{t1}/P_{t0} was computed for each model. For comparative purposes, the ratio of the average total pressure loss across the test section for each injector ramp model was normalized by that of the no-ramp transverse injection. A total pressure loss parameter was then defined as

$$\Pi = (P_{t1}/P_{t0})/(P_{t1}/P_{t0})_{\mathrm{NR}} \tag{1}$$

where an average value was computed over the measurement domain. Accounting for probe location, transducer calibration, and number of samples indicated a 3.0 and 13.0% uncertainty in the Mach number and total pressure, respectively. Because 1250 samples (across the plume) were used in the evaluation of the total loss parameter [Eq. (1)], the uncertainty was expected to be significantly lower than the 13% for the point measurement. Assuming that the variance was equal to the product of the percent uncertainty and the mean estimate, the 99% confidence interval was calculated as 1.0%.

The digital two-color particle image velocimetry system described in Dasgupta et al.[17] was used to obtain the Mie scattering

images. Two Surelite Nd:YAG lasers and a single Raman cell were used to produce 532-nm (green) and 607-nm (red) wavelength laser beams. A cylindrical lens was used to produce the laser sheet. The width of the laser sheet had an hourglass shape, where the maximum thickness at the top and bottom of the wind tunnel was measured as roughly 0.7 mm, and the waist thickness was estimated as 0.3 mm. The pulse duration of each laser was 10 ns. The two lasers were pulsed 300 ns apart at a rate of 10 Hz. A Kodak Model 460C charged coupled device camera, with a Nikon N90 lens, was used to capture the images. The jet flow was seeded with triethylene glycol smoke particles that were generated with a Dantec brand fog generator. The fog generator produced a polydisperse particle distribution, where the particle diameters are generally accepted to be 2–4 μm. Because of the complex dependency of Mie scattering on particle size and viewing angle, it is conservatively expected that only the larger particles were imaged. Hence, the present quantitative analysis was restricted to measuring the peak mean penetration and cross-sectional area. In addition, an analysis of the intensity decay rate was also performed to qualitatively assess relative changes in the mixing rates.

For the instantaneous images, the camera exposure time was set to 0.125 s, with an f-stop setting of 5.6, and thus, one 10-ns pulse from each laser was captured. The time-averaged images were obtained by setting the exposure time to 4 s, at an f-stop of 16, and capturing 80 pulses (40 from each laser) on a single image.

Images were obtained both parallel and perpendicular to the jet flow. The parallel-oriented laser sheet was aligned along the tunnel centerline, parallel to the $x-y$ plane, and sized to cover 6.5 cm measured from the front lip of the injector nozzle exit. The laser intensity was visibly uniform from just in front of the injector port to $16d$ downstream of the injector ($4d$ upstream of the mean flow measurement plane). For the crossflow-oriented images, the laser sheet was oriented perpendicular to the flow at the same axial position as for the mean flow measurements, and the camera was situated 26-deg off-axis.

Visual estimates of the maximum penetration (y_m) profile and digital measures of the jet intensity decay rates were acquired from the mean side-view images. The outermost visible plume edge was used to define the maximum penetration. The peak penetration measurements were hindered by the low-intensity, oscillatory nature of the outermost plume edge. The peak-to-peak oscillations were measured as roughly 5% of the peak penetration. Hence, the uncertainty in the maximum mean penetration was estimated, based on this analysis, as 5%. The uncertainty with the measurement device was negligible (< 0.5%) compared with the plume edge oscillations. It is also noteworthy that the mean penetration measurements were repeatable on a photograph-to-photograph comparison to within 2.0%.

To qualitatively assume that the intensity decay rates were proportional to injectant concentration decay rates, it was necessary to assume that the concentration decay rate caused by the plume spreading dominated over the mean density change as a result of the acceleration of the jet. This assumption was reasonably away from the jet exit, where the static pressure and total temperature were roughly constant and the velocity change was relatively mild. Hence, the concentration decay rate estimates were limited to an x/d range of 5.0–16.0. The results were arbitrarily scaled to 1.0 at the first data point. Again, because of the larger seed particles not tracking the small-scale motions and the preceding assumption, the intensity concentration decay rate analysis provided qualitative insight only.

Plume areas and maximum penetration at $x/d = 20$ were estimated from the cross-sectional images by assuming an elliptical cross section and visually measuring the major and minor axes. For performance-enhancement assessment purposes, it was assumed that the mixing rates would roughly scale with the plume area. As for the case of side images, the fluctuations noticed in the plume edge definitions were estimated as 5% of the plume dimension. Hence, the estimated uncertainties based on this analysis were 5 and 10% in the peak penetration and plume area, respectively. The plume area and maximum penetration measurements were repeatable to within less than half of the measurement uncertainty, 5.0 and 2.0%, respectively.

Results and Discussion

Shadowgraph Flow Visualization

Figure 3 presents composite shadowgraphs for the no-ramp, double-ramp, tapered-ramp, and wide-ramp flows. A strong bow shock was created as the plume entered the freestream (located just below the ceiling boundary layer and slightly ahead of the injection point). For all four cases, the plume bow shock started at an angle of ~33 deg, and then bent over to approximately 25 deg by the middle of the test section. All three ramps (Figs. 3b–3d) created a compression shock system that coalesced with the plume bow shock near the vertical midpoint of the test section. The angle of the compression shock structures was ~35 deg. As expected, the double ramp created the strongest shock structure. The flow recompression shocks are also visible on each of the four shadowgraphs, where again, the two-dimensional double ramp produced the strongest shock. The shadowgraphs indicated that all of the downstream ramps produced only weak additional shock structures, and thus, minimal increases in shock-induced total pressure loss as compared with the no-ramp case.

Mie Scattering Flow Visualizations

The Mie scattering instantaneous side, time-averaged side, and time-averaged cross-sectional views for the four injector configurations are shown in Figs. 4a–4d. The instantaneous side-view images depict the large-scale vortical structures just beyond the fold over the region where the jet bends to be coaxial with the freestream. The

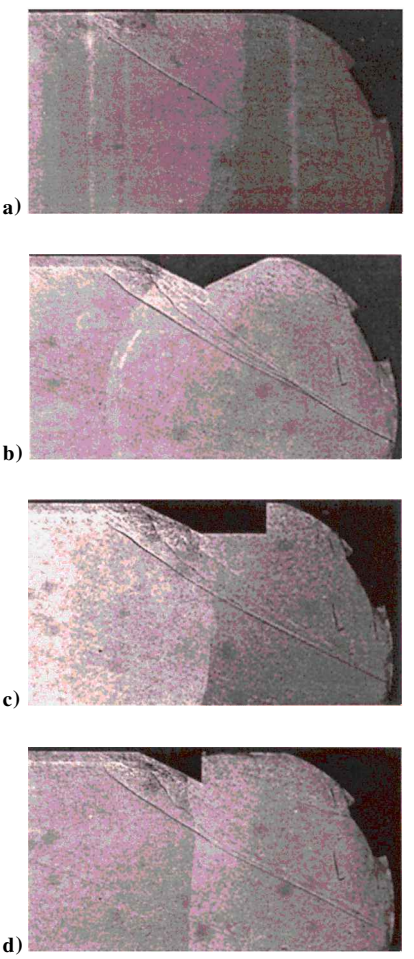

Fig. 3 Shadowgraph photographs: a) no ramp, b) double ramp, c) tapered ramp, and d) wide ramp.

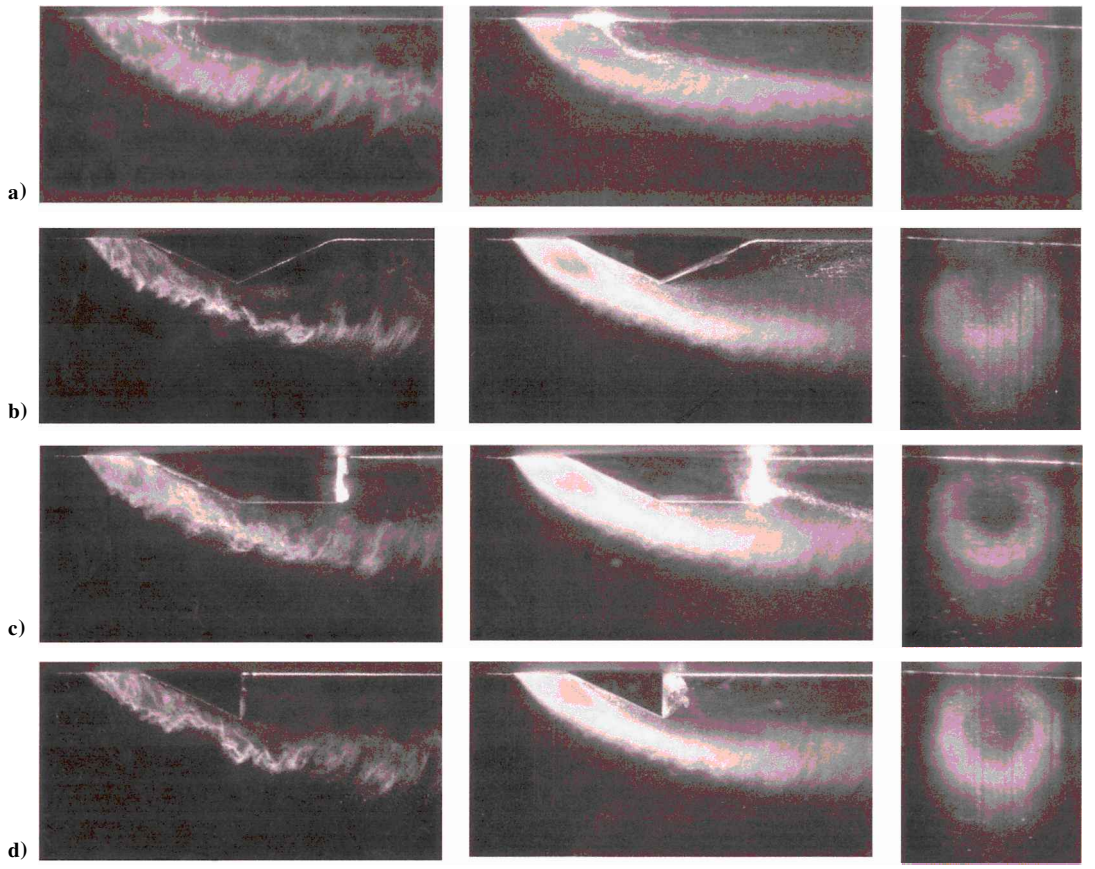

Fig. 4 Mie scattering images (left to right) of instantaneous streamwise, average streamwise, and average cross-sectional views for a) no-ramp, b) double-ramp, c) tapered-ramp, and d) wide-ramp flow models.

ramps seem to have reduced the organized nature of the large-scale structures seen in Fig. 4a. The large-scale motions and jet-plume unsteadiness become apparent when the mean and instantaneous side-view images were compared. The injector barrel shock region is also visible in the time-averaged side views for all four configurations, where the presence of the ramps moved the Mach disk upstream as compared with the no-ramp case.

Recall that the ramp angles were designed to match the injection angle, and that increased penetration was expected from the Magnus force and bulk compression. The apparent separation between the plume and the ramp compression faces, noticeable in the instantaneous and time-averaged side-view images, indicated that liftoff, and thus, increased penetration, was indeed created by the ramps. The visually extracted maximum penetration heights from the mean Mie scattering side-view images confirmed that the penetration was enhanced (see Fig. 5). The first group of data points ($x/d < 16$) were obtained from the mean side-view Mie images, and the last data point ($x/d = 20$) was measured from the cross-sectional view. As can be seen, all of the ramps increased the centerline penetration, where the double ramp produced the deepest penetration (22% increase over the no-ramp case at $x/d = 20$). As mentioned in the Instrumentation and Data Analysis section, the estimated uncertainty for the penetration plots are nominally 5%. Hence, the differences in the peak penetration are roughly twice the uncertainty. The slopes of the logarithmic curve fits were larger for each of the three ramps as compared with the no-ramp case, which indicated the potential for increased far-field penetration. The $x/d = 20$ penetration measurements for all seven ramps are summarized in Table 2. A complete discussion of the data summarized in Table 2 is given in the Performance Comparisons section.

Peak concentration decay rates have often been used to compare the mixing efficiency of fuel-injection schemes. The qualitative estimates of the average plume centerline ($z/d = 0$) intensity, as estimated from the time-averaged side-view Mie images (Fig. 4), are

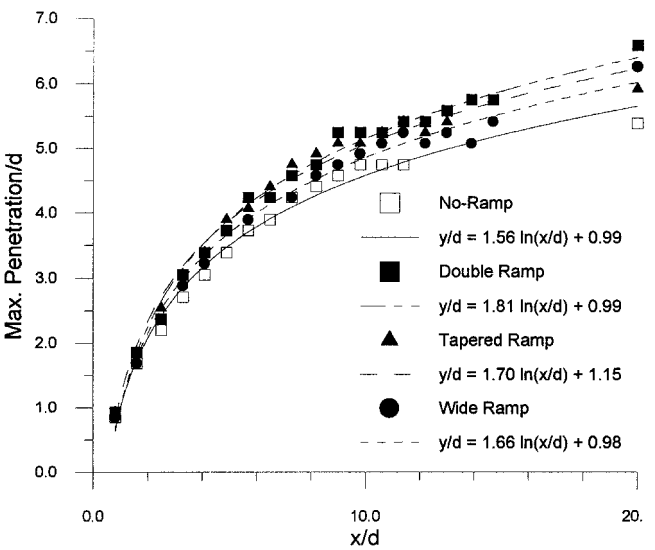

Fig. 5 Maximum penetration x/d (5.0% measurement uncertainty).

plotted vs x/d in Fig. 6. As indicated in Fig. 6, the average centerline intensity decreased more rapidly with the ramps present. Using the slope of a linear fit as a qualitative indicator of increased decay rates, the double ramp produced the largest increase in the decay rate (27% increase over the no-ramp case). The slight increase in the no-ramp injection at $x/d = 6$ was the result of the barrel shock region, where the intensity was slightly lower, extending slightly farther downstream for this case. The decay rates for all seven ramps shown in Fig. 2 are given in Table 2.

As the sample set of cross-sectional images in Fig. 4 indicates, the presence of the ramps also had a profound impact on the plume

Table 2 Injector performance parameters

Injector	Group[a]	A_b/d^2	$\bar{P}_{t1}/P_{t0}$	Π	A_p/d^2	y_m/d	D	ξ_y	ξ_A	ξ_D	Vorticity
No ramp	——	——	0.81	1.00	23.0	5.4	−0.049	——	——	——	Strong
Double ramp[b]	I	18.8	0.67	0.83	32.0	6.6	−0.062	1.3	2.3	1.6	Weak
Tapered ramp[b]	II	14.1	0.69	0.85	28.0	6.2	−0.060	1.0	1.4	1.5	Strong
Wide ramp[b]	III	14.1	0.71	0.88	29.0	6.2	−0.052	1.2	2.2	0.5	Strong
Double diamond	I	9.4	0.78	0.96	25.0	6.0	−0.051	2.8	2.2	1.0	Strong
Double cone	I	14.8	0.74	0.91	28.0	6.2	−0.058	1.6	2.4	2.0	Strong
Truncated ramp	II	15.3	0.74	0.92	26.0	5.9	−0.054	1.2	1.6	1.3	Strong
Narrow ramp	III	11.8	0.71	0.88	26.0	6.2	−0.052	1.2	1.1	0.5	Strong

[a]See Fig. 2. [b]Three ramps highlighted in this paper.

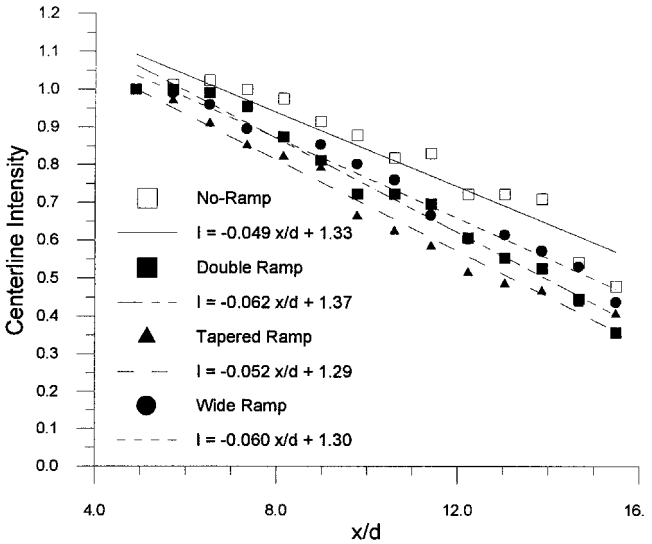

Fig. 6 Qualitative estimates of the centerline average intensity.

cross-sectional size and shape. The cross-sectional images clearly depict the expected cardioidal shape of the plume. Using the cardioidal shape of the plume as a qualitative indication of the vortex pair strength, it was apparent that the vorticity was strongest for the tapered ramp case and weakest for the double-ramp injector. This trend suggests that the ramp sweep increased the vorticity, as expected. The reduced vorticity for the wide ramp indicates that the expansion generated at the ramp apex strongly influences the vorticity transport through the baroclinic torque, where the expansion strength was expected to be weaker for the tapered ramp. The Mach number contours discussed next enforce the plume vorticity trends. The plume area was visibly larger for all three ramps as compared with the no-ramp case, where the double-ramp plume was the largest (a 39% increase over the no-ramp plume) at $x/d = 20$. Even though the double ramp demonstrated superior mixing, i.e., the largest plume, at $x/d = 20$, the wide and tapered ramps were designed to increase the vorticity, and thus, the far-field performance. Based on previous comparisons between physical ramps and flush-wall injectors (discussed in the Introduction), where vorticity was shown to be the driving mixing mechanism, it is expected that the far-field performance ($x/d \sim 100$) of the wide and tapered ramps will be better than that of the double-ramp. The estimated plume areas for all seven ramps are summarized in Table 2.

Mach Number Contours

The Mach number contours at $x/d = 20$ for the no ramp, double ramp, tapered ramp, and wide ramp are presented in Fig. 7. The contours are oriented such that the flow is into the page and the injector is located at the bottom.

The Mach number contour plot for the simple transverse injection case is shown in Fig. 7a. The expected plume and flow structures are observable in the contour plots. The plume is readily discernible at the bottom-center of the plot. The contour plot shows that the plume had the roughly circular shape seen in cross-sectional Mie images (Fig. 4a). Inside the plume, the twin cores of the counter-rotating vortex pair are clearly visible in the Mach contour. Outside the plume, the secondary conical recompression shock is visible, encircling the plume as an arching structure that peaks at about $y/d = 6.0$. The large arcing structure centered near $(y/d, z/d) = (10, 0)$ is the bow shock that was created by the injection plume. The structure seen spreading from y/d of ~7.0–11.0 at z/d of ±5.6 is the plume shock side-wall boundary-layer interaction. The tunnel ceiling boundary-layer height (along the bottom of the plot) varied from $\sim y/d = 1.6$ at the outside edges to $y/d = 1.0$ in the plume area.

The Mach number contour plot for the double ramp is given in Fig. 7b. The vortex core of the double ramp differed substantially from the simple transverse injection. The plume core region appeared to be more like a single stream tube into the page rather than the usual twin vortex core system. Apparently, the two-dimensional shock and expansion waves from the double ramp caused a breakdown of the vortex structure. As expected, the double-ramp shock had a relatively flat midsection, and steeper sloped sides. The horseshoe vortices generated by the double ramp are clearly noticeable in the boundary layer near $z/d = \pm 1.0$. The downstream recompression shock is noticeable as the weak arching structure centered near $y/d = 7.0$, $z/d = 0.0$.

The Mach number contour plot for the tapered ramp is given in Fig. 7c. The apparent large strength of the plume vortices was the product of the vorticity generated by spillage over the ramp compression face. As the flow travels to the end of the tapered extension, the narrow trailing edge effectively drove the vortices into each other, resulting in a narrow separation. The tapered ramp recompression shock was substantially more rounded than that of the double ramp. Overall, the flow structures depicted in the Mach number contour for the wide ramp (Fig. 7d) are somewhat similar to those of the tapered ramp, with the exception of the larger and more widely plume vortices of the wide ramp. This result indicates that as the flow spills around the tapered ramp, it travels parallel to the taper. Thus, the two plume vortices impacted with each other at the trailing edge, resulting in vertical trailing-edge shocks and a more compact plume as compared with the wide ramp.

The total pressure contours were computed, using the normal shock relations, from the data in Fig. 7 and the pitot pressure data. The contours were qualitatively similar in structure to the Mach number contours, and hence, they were not reproduced here. The average total pressure loss [Eq. (1)] are included in Table 2, and discussed in the next section.

Performance Comparisons

The previous sections indicated that the presence of the ramps significantly increased the penetration and mixing of the jet plume within the high-momentum freestream. Throughout the analysis of the data, a number of parameters were selected to use as a basis of comparison between the injector configurations. The ramp geometry (size and shape) had a major impact on the plume structure. The average total pressure loss [Eq. (1)] was used to assess the losses associated with each model. Because the jet and tunnel flow total conditions were held constant to within 2.0%, it was assumed that an increased plume cross section indicated an increase in freestream air within the plume, which would result in an increased potential for turbulent diffusion. Thus, based on this simplistic model, mixing efficiency was assumed to scale with the plume area, as estimated

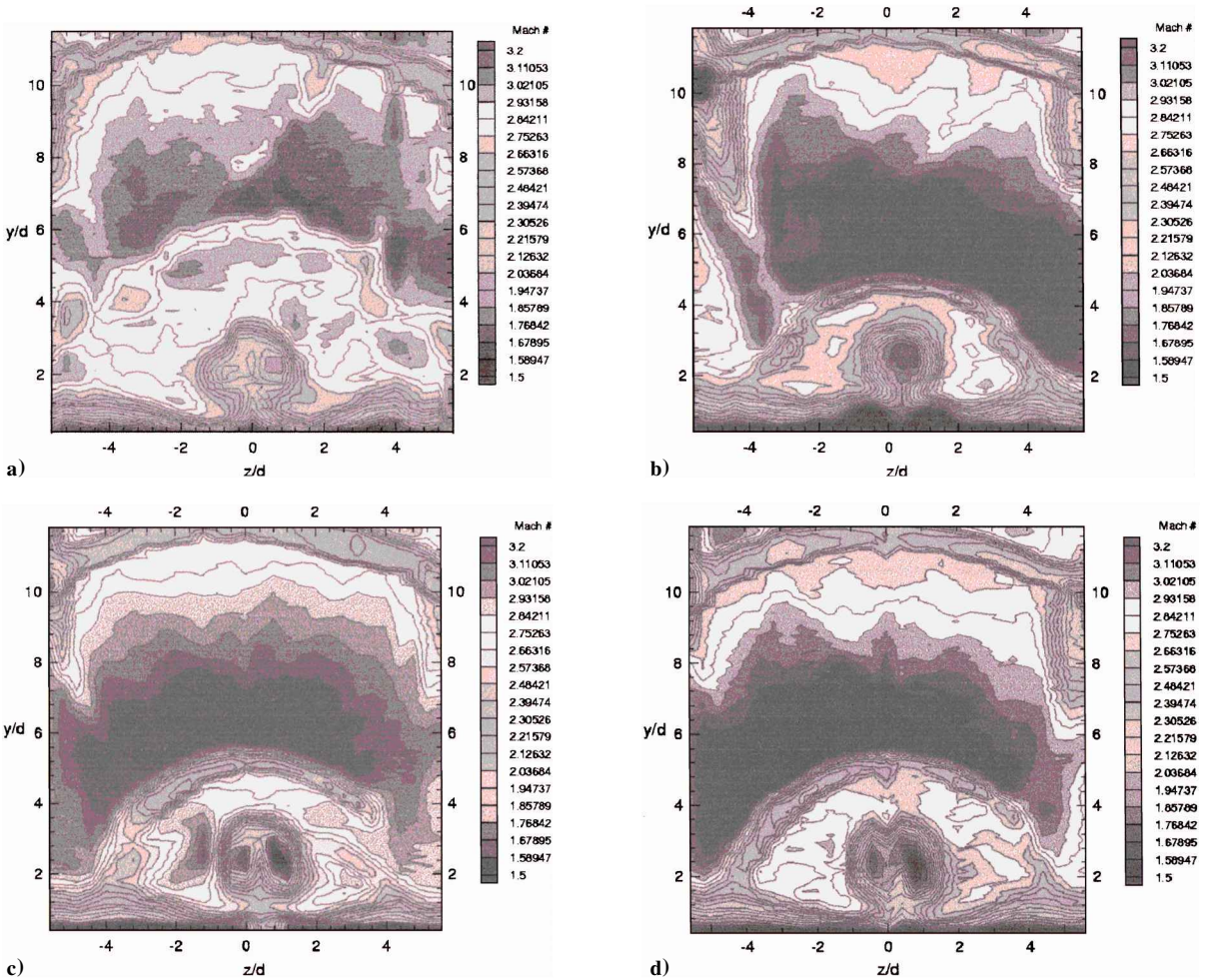

Fig. 7 Mach number and total pressure contour plots (x/d = 20): a) no ramp, b) double ramp, c) tapered ramp, and d) wide ramp.

from the mean Mie scattering images. The centerline average seed concentration decay rate was assumed to be representative of the plume maximum, and thus, indicative of mixing. The ramp geometry and estimated performance parameters for all eight injectors are summarized in Table 2. The parameters listed in Table 2, proceeding from left-to-right, include ramp group, ramp blockage area, average total pressure loss across the test section, normalized average total pressure loss, plume area at $x/d = 20$, maximum plume penetration at $x/d = 20$, mean centerline decay rates, and figure-of-merit estimates (discussed in the next paragraph). Vortex strength is important for far-field mixing; hence, a qualitative indication of the vortex-pair strength (strong or weak), based on the cardioidal structure of the plume, is listed in the last column of Table 2.

All of the ramps increased the penetration and plume area, where the double ramp produced the largest plume and deepest penetration. On the other hand, all of the ramps resulted in a decrease in the total pressure, where the double ramp created the largest total pressure loss. Adding drag to the combustor is a severe penalty in overall engine efficiency that results from adding the ramps to the combustor. However, the observed increased mixing and penetration will result in a shorter combustor, which may offset the drag penalty and increase the overall engine efficiency; this will ultimately lead to a design-optimization problem.

To account for total pressure loss in comparing the ramps, a figure-of-merit (ξ) was defined as the percent change in improvement of a mixing or penetration parameter divided by the percent change in total pressure loss as compared with the no-ramp case. The plume area, maximum penetration, and decay rate figure-of-merit data are summarized in Table 2.

Overall, the symmetric ramps (group I) produced, on the average, the largest gains in performance at $x/d = 20$, with the lowest losses in total pressure. The group I figure-of-merit data indicate that if the size of the double-diamond or double-cone cross sections were increased to the point where total pressure loss was equivalent to that of the double ramp, then the magnitude of the performance improvement would be comparable. However, it is noteworthy that the total pressure loss does not necessarily scale with the blockage area alone; ramp geometry is also important. For example, the tapered ramp had a frontal blockage that was 8.5% larger than that of the truncated ramp; however, the total pressure loss was 8.2% lower and the figure-of-merits were similar. The larger taper angle of the tapered ramp as compared with the truncated ramp produced stronger vertical shock waves at the trailing edge of the ramp as compared with the truncated ramp; hence, the lower total pressure loss for the truncated ramp was not overly surprising. Based on previous comparisons between physical ramps and flush-wall injectors, where vorticity was shown to be the driving mixing mechanism, it is expected that the far-field performance of the wide and tapered ramps will be better than that of the double ramp, where again, the wide ramp had a lower total pressure loss.

Interestingly, the good performance measures noticed for the wide ramp were not shared by the narrow ramp. It is expected that the reduced size of the leading-edge compression face significantly reduced the influence of the ramp on the plume dynamics. Even though the sweep produced spillage-generated vorticity, the larger taper resulted in a more compact plume. Moreover, the narrow ramp frontal blockage area was 16% smaller than that of the wide ramp, but the total pressure loss was the same for the two ramps.

The data in Table 2 indicate that ramps can be designed to provide a passive means to increase the performance of a scramjet fuel injector, where trades between mixing, penetration, total pressure loss, combustor length, and weight can be performed. The jet–ramp interaction enhancement mechanisms include baroclinic torque-created vorticity, ramp spillage-generated vorticity, bulk compression and the Magnus force. The structure of the turbulence associated with the jet flow, which is strongly dependent on the secondary vortex motions[18] and a key factor in mixing efficiency, will also be influenced by the PME ramps. The data summarized in Table 2 provides trends that can be used to narrow the design space for more detailed analyses aimed at ramp optimization.

Conclusions

The primary objective of this investigation was to examine the effectiveness of downstream ramps to control the penetration and mixing of a supersonic gaseous injection into a supersonic freestream. Mie scattering flow visualization, shadowgraph photography, and conventional mean flow probes were used to document the plume characteristics for seven ramps designed to examine specific performance enhancement features. The present data indicated that the interaction between the inherent plume flow features and the ramps significantly increased the penetration and plume expansion (~mixing) of the jet plume; thus, providing a method to passively control the performance of a scramjet fuel injector. The potential jet–ramp interaction enhancement mechanisms include baroclinic torque-created vorticity, ramp spillage-generated vorticity, bulk compression, and the Magnus force.

Of the ramps tested, the symmetric ramps produced the best gains in performance with the lowest decreases in total pressure at $x/d = 20$. Based on previous comparisons between physical ramps and flush-wall injectors, where vorticity was shown to be the driving mixing mechanism, it is expected that, because of the strong vortex pair of the wide ramp, the far-field performance will be better than that of the double ramp, where the vortex pair was destroyed. The symmetric ramps demonstrated that ramp blockage was an important factor in determining the performance enhancement and total pressure loss. In addition, the extended and asymmetric ramps showed that the ramp geometry also had a large impact on the magnitude of the performance gain and total pressure loss. In summary, the present PME ramps produced 13–39% increases in total plume area (~mixing efficiency), 9–22% increases in penetration, 4–27% increases in the average centerline concentration decay rate, and 4–17% decreases in total pressure. Thus, significant performance improvements were demonstrated where two-to-one gains in performance over total pressure loss (figure-of-merits) were achieved. In summary, the present study demonstrated that downstream ramps can be used to alter the jet plume characteristics, and the results provide trends that can be used to narrow the design space for more detailed analyses aimed at ramp optimization.

Acknowledgments

The authors gratefully thank A. Nejad (Wright Laboratory); M. Gruber (Wright Laboratory); L. Goss (Innovative Scientific Solutions, Inc.); S. Gogoneni (Innovative Scientific Solutions, Inc.); T. Chen (Taitech, Inc.); and S. Dasgupta (Taitech, Inc.), for providing technical support and the Mie flow visualization equipment used in this study.

References

[1]Schetz, J., Hawkins, P., and Lehman, H., "The Structure of Highly Underexpanded Transverse Jets in a Supersonic Stream," *AIAA Journal*, Vol. 5, No. 5, 1967, pp. 882–884.

[2]Schetz, J., and Billig, F., "Penetration of Gaseous Jets Injected into a Supersonic Stream," *Journal of Spacecraft and Rockets*, Vol. 3, No. 11, 1966, pp. 1658–1665.

[3]Hollo, S., McDaniel, J., and Harfield, R., "Quantitative Investigation of Compressible Mixing: Staged Transverse Injection into Mach 2 Flow," *AIAA Journal*, Vol. 32, No. 3, 1994, pp. 528–534.

[4]Grasso, F., and Magi, V., "Simulation of Transverse Gas Injection in Turbulent Supersonic Air Flows," *AIAA Journal*, Vol. 33, No. 1, 1995, pp. 56–62.

[5]Waitz, I. A., Marble, F., and Zukoski, E., "Investigation of a Contoured Wall Injector for Hypervelocity Mixing Augmentation," *AIAA Journal*, Vol. 31, No. 6, 1993, pp. 1014–1021.

[6]Riggins, D., McClinton, C., Rogers, R., and Bittner, R., "Investigation of Scramjet Injection Strategies for High Mach Number Flows," *Journal of Propulsion and Power*, Vol. 11, No. 3, 1995, pp. 409–418.

[7]Schetz, J., Thomas, R., and Billig, F., *Mixing of Transverse Jets and Wall Jets in Supersonic Flow*, Springer–Verlag, Berlin, 1991.

[8]Fuller, R., Wu, P.-K., Nejad, A., and Schetz, J., "Fuel-Vortex Interaction for Enhanced Mixing in Supersonic Flow," AIAA Paper 96-2661, July 1996.

[9]Riggins, D., and Vitt, P., "Vortex Generation and Mixing in Three-Dimensional Supersonic Combustors," *Journal of Propulsion and Power*, Vol. 11, No. 3, 1995, pp. 419–425.

[10]Hartfield, R., Hollo, S., and McDaniel, J., "Experimental Investigation of a Supersonic Swept Ramp Injector Using Laser-Induced Iodine Fluorescence," *Journal of Propulsion and Power*, Vol. 10, No. 1, 1994, pp. 129–135.

[11]Donohue, J., McDaniel, J., and Hossein, H.-H., "Experimental and Numerical Study of Swept Ramp Injection into a Supersonic Flowfield," *AIAA Journal*, Vol. 32, No. 9, 1994, pp. 1860–1867.

[12]Northam, G., Greenberg, I., Byington, C., and Capriotti, D., "Evaluation of Parallel Configurations for Mach 2 Combustion," *Journal of Propulsion and Power*, Vol. 8, No. 2, 1992, pp. 491–498.

[13]Abramovich, G., *The Theory of Turbulent Jets*, MIT Press, Cambridge, MA, 1960.

[14]McCann, G., and Bowersox, R., "Experimental Investigation of Supersonic Gaseous Injection into a Supersonic Freestream," *AIAA Journal*, Vol. 34, No. 2, 1996, pp. 317–323.

[15]Volluz, R., *Handbook of Supersonic Aerodynamics, Section 20, Wind Tunnel Instrumentation and Operation*, Vol. 6, Ordnance Aerophysics Lab., NAVORD Rept. 1488, Daingerfield, TX, 1961.

[16]Wilson, M., *Experimental Investigation of Transverse Supersonic Injection Enhancement into Supersonic Flow*, AFIT/GAE/ENY96D-08, MS Thesis, Air Force Inst. of Technology, Wright–Patterson AFB, OH, Dec. 1996.

[17]Dasgupta, S., Terry, W., Vappuladhadium, R., Bowersox, R., Glawe, D., and Nejad, A., "A Two-Color Particle Image Velocimetry System for Supersonic Flow Studies," AIAA Paper 96-2798, July 1996.

[18]Bowersox, R., "Turbulent Flow Structure Characterization of Angled Injection into a Crossflow," *Journal of Spacecraft and Rockets*, Vol. 34, No. 2, 1997, pp. 205–213.